M.C. CHEN
J.Y. HUANG✉
L.J. CHEN

Coherent control multiphoton processes in semiconductor saturable Bragg reflector with freezing phase algorithm

Department of Photonics and Institute of Electro-Optical Engineering, Chiao Tung University, Hsinchu, Taiwan, R.O.C

ABSTRACT A freezing phase concept has been proposed for adaptive coherent control with a femtosecond pulse shaper. We applied the scheme to investigate multiphoton processes in InAs quantum dot saturable Bragg reflector (SBR). The optical transition of InAs quantum dots can be revealed in the spectral phase sensitivity plot of second harmonic signal. We also achieved a three-time increase in image contrast on regions with photoluminescent wavelength differing only 18 nm by using coherent control nonlinear optical microscopy. Our results suggest the new freezing phase scheme to be useful for various investigations which require fast and reliable complete-field characterization and coherent control on one setup.

1 Introduction

An attractive scheme to control the quantum evolution of a complex system is via adaptive laser pulses control [1–4]. In this regard, several algorithms have been developed to tailor a coherent optical field for preparing specific products on the basis of fitness information [5–10]. The question remained is whether the optimal laser field contains a set of rational rules that govern the dynamics. Recent study suggests that the answer could be affirmative [11]. Therefore, the purpose of femtosecond coherent control study is not only to control the evolution of a complex system but also to deduce the detailed dynamic mechanism from the optimal laser field used.

Coherent control technique has been demonstrated with femtosecond laser pulse shaper with spatial light modulation (SLM) devices [12, 13]. The only pulse shaping method with conserved pulse energy is to adjust spectral phase for tailoring the pulse shape [14–19]. For practical applications, it is highly desirable to integrate optical field characterization and adaptive coherent control into one apparatus. With the setup the desirable optical field characteristics can be verified and be used

to selectively excite one type of probe molecule while leave the others in their ground state [4]. Contrast enhancement via coherent control and functional imaging of samples labeled with environment-sensitive fluorescent probes can therefore be realized.

InAs quantum dots (InAs-QDs) in a Bragg reflector (SBR) structure have important applications for ultrafast optical shaping at $1.3\,\mu\text{m}$. SBR usually consists of a highly reflective Bragg mirror and quantum well or quantum dots embedded in it [20]. Under conditions of strong excitation, the absorption is saturated because initial states of the transition are depleted while the final states are partially occupied. It is important to properly position the saturable semiconductor layer to control saturation fluence of the device. In this paper, we report an effective pulse shaping scheme for complete-field characterization and adaptive coherent control of multiphoton processes with one setup.

This paper is organized as follows: in Sect. 2, we first illustrate the principle and operational procedure of the freezing phase scheme. We then apply the scheme to theoretically deduce the optimal spectral phase profile for two-photon excitation with or without intermediate resonant level. Experimental details about the optical characteristics of a SBR device used are presented in Sect. 3. Results about coherent and incoherent multiphoton processes, spectral-phase sensitivity study of various multiphoton signals, and coherent control microscopy of the SBR are presented in Sect. 4. Finally conclusion is drawn.

2 Theoretical analysis

To illustrate the freezing phase algorithm (FPA), we express a coherent optical field in terms of its spectral components:

$$E(t) = \sum_{n=0}^{N} A_n \exp\left[\,j\,(\omega_0 + 2\pi\,n\,\Delta\nu_{\text{F}})\,t + \phi_n\,\right]. \tag{1}$$

Here ω_0 is the optical carrier frequency, $\Delta\nu_{\text{F}}$, ϕ_n and A_n denote the frequency span, phase constant, and amplitude of the spectral components, respectively.

In a typical 4-f pulse shaping setup shown in Fig. 1, the pulse spectrum is first angularly dispersed with a grating

✉ Fax: +886-3-5716631, E-mail: jyhuang@cc.nctu.edu.tw
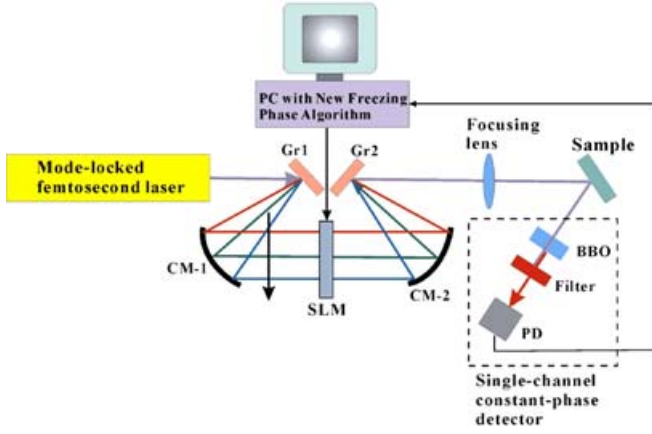
FIGURE 1 Schematic of an adaptive pulse shaping setup used in this study. The apparatus is comprised of an all reflective 4-f pulse shaper. Here Gr1 and Gr2 denote a pair of gratings, CM-1 and CM-2 two concave reflectors with 10-cm focal length, SLM one-dimensional pixelated spatial light modulator, BBO a 3-mm thick type-I β-Ba$_2$BO$_4$ second-harmonic crystal, and PD a photodiode detector

Gr1 [19]. Each pixel m in a one-dimensional pixel-like spatial light modulator (SLM) can accommodate spectral components from K_m^0 to K_m^t. We can impose a phase retardation pattern φ_m on a M-pixels SLM and transforms the input coherent field into a shaped output

$$E(t) = \sum_{m=1}^{M} \sum_{k=K_m^0}^{K_m^t} B_k \exp\left[j\left(\omega_0 + 2\pi k \Delta\nu_F\right) t + \phi_k + \varphi_m\right],$$

(2)

where the ratio of B_n/A_n denotes the field transmittance of the nth pixel. Equation (2) indicates that the amplitude of the shaped pulse $E(t)$ reaches a peak value E_p at $t_p = K/\Delta\nu_F$ (where $K \in$ integer)

$$E_p = \exp\left(i\omega_0 t_p\right) \sum_{m=1}^{M} \sum_{k=K_m^0}^{K_m^t} B_k \exp\left[i\left(\phi_k + \varphi_m\right)\right].$$

(3)

We arbitrarily choose pixel j from the SLM and use it as a phase modulation component by varying its phase retardance. The remaining M-1 pixels serve as the reference and by defining

$$C_j \exp\left(i\theta_j\right) = \sum_{m=1}^{j-1} \sum_{k=K_m^0}^{K_m^t} B_k \exp\left[i\left(\phi_k + \varphi_m\right)\right]$$

$$+ \sum_{m=j+1}^{M} \sum_{k=K_m^0}^{K_m^t} B_k \exp\left[i\left(\phi_k + \varphi_m\right)\right]$$

$$D_j \exp\left(i\vartheta_j\right) = \sum_{k=K_j^0}^{K_j^t} B_k \exp\left[i\left(\phi_k + \varphi_j\right)\right],$$

(4)

the peak intensity I_p can be expressed as

$$I_p = |E_p|^2 = C_j^2 + D_j^2 + 2C_j D_j \cos(\theta_j - \vartheta_j).$$

(5)

The first two terms represent the spectral intensities of the reference and the phase modulation component. The third term denotes interference between the two components. Note that I_p can achieve a maximum with $\theta_j = \vartheta_j$. By successively adjust every spectral component we can guide all spectral components toward a "frozen phase state", where the shortest pulse can be produced.

2.1   *Freezing phase procedure for second harmonic generation*
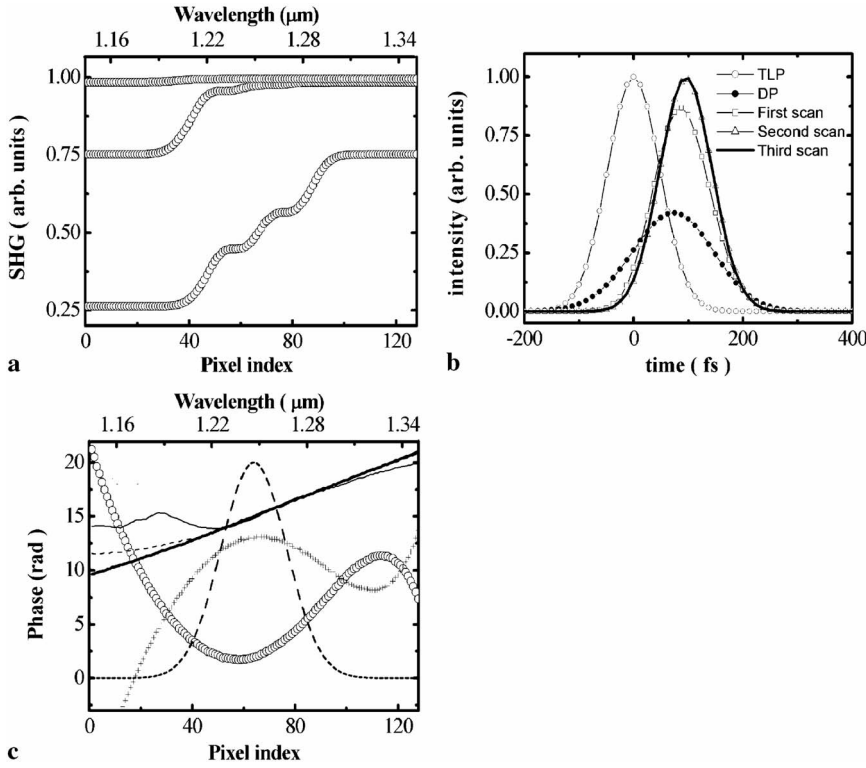
We first perform a model simulation in order to verify the functionality of our freezing phase procedure. The input coherent optical pulse is assumed to have a Gaussian profile with 50 fs of FWHM pulse duration and 1.252 μm of central wavelength. The coherent pulse is distorted with a phase profile of $15[(i-64)/64]^2 + 7[(i-64)/64]^3 - 7[(i-40)/64]^4 - 8[(i-60)/64]^5$, where $i = 1, 2, \ldots,$ M denotes the position index of the SLM pixels.

Our simulation starts by dividing the SLM pixels into two groups: We arbitrarily pick up one pixel to serve as phase modulation and the remaining M-1 pixels form a reference group. We vary the phase of the modulation pixel from 0 to 2π to produce SH intensity variation with a SHG crystal. For coherent control applications, two to three times of phase adjustment are usually sufficient to yield the information about the correct phase retardation of the modulation pixel for the frozen phase state. We set the modulation pixel to this phase retardation and the procedure is repeated by scanning phase modulation pixel over SLM until the phase retardations of all pixels have been properly adjusted.

The intensity profile of the input distorted pulse is presented in Fig. 2b with filled circles. The corresponding spectral phase profile is shown in Fig. 2c with open circles. The phase-freezing procedure was implemented by scanning SLM pixels from left to right side to compensate for the distorted phase profile. Figure 2a shows the time course of the maximum value of spectrally integrated SH signal yielded during the phase-freezing process. The SH signal had been normalized to that with transform-limited pulse (TLP).

We note that significant SH signal changes always occur at those SLM pixels lying within the spectral range (i.e., 1.20 μm → 1.29 μm) of the input pulse. SH intensity can reach 75% of the transform-limited value after the first scan and 98% after the second scan.

The corresponding pulse profiles after the first (open squares), the second (open triangles) and the third freezing phase scan (thick solid curve) are presented in Fig. 2b. The pulse spectrum (dashed curve), the distorted phase (DP, open circles), the compensating phase (CMP, cross symbols), and the error phase obtained from a summation of DP and CMP are shown in Fig. 2c. After the first scan, the root-mean-squared (rms) deviation of the error phase from a linear-phase decreases to 1.995. The deviation can be further reduced to 0.640 by the second phase freezing scan and to 0.095 by the third scan. We shall point out that a linear phase in frequency domain simply results in a shift (see Fig. 2b) of the entire pulse in time domain. Thus from the time invariance principle, our phase retrieval method does not miss any information about pulse characteristics.

2.2 Freezing phase procedure for two-photon absorption process

Silberberg et al. had pointed out that owing to the appearance of resonant intermediate levels the optimal pulse profile for generating maximal two-photon fluorescence (TPF) is not transform-limited [21]. To show the wide applicability of our freezing phase scheme, we further apply our FPA to a two-photon absorption (TPA) process with an energy-level structure detailed in Fig. 3a.

We excite TPA with an ultrashort laser pulse $E(t)$. By invoking the second-order time-dependent perturbation theory, the amplitude of the TPA transition via an intermediate level $|i\rangle$ can be derived to be [21]

$$a_f^r \approx -\frac{1}{i\hbar^2} \sum_i \mu_{fi}\mu_{ig} \left[i\pi \, E(\omega_{ig}) E(\omega_{fg} - \omega_{ig}) \right.$$

$$\left. + \wp \int_{-\infty}^{+\infty} \frac{E(\omega) E(\omega_{fg} - \omega)}{\omega_{ig} - \omega} d\omega \right], \qquad (6)$$

where $E(\omega) = FT[E(t)] = A(\omega) \exp[i\Phi(\omega)]$, and $\wp$ denotes the Cauchy principle value integral. We apply FPA to maximize the two-photon transition probability by adjusting the spectral phase $\Phi(\omega)$ of the input ultrashort pulse. Two intermediate levels are assumed to lie at 1247 nm and 1273 nm, which are within the spectral range of the input pulse. We compare the FPA result to that with genetic algorithm (GA).
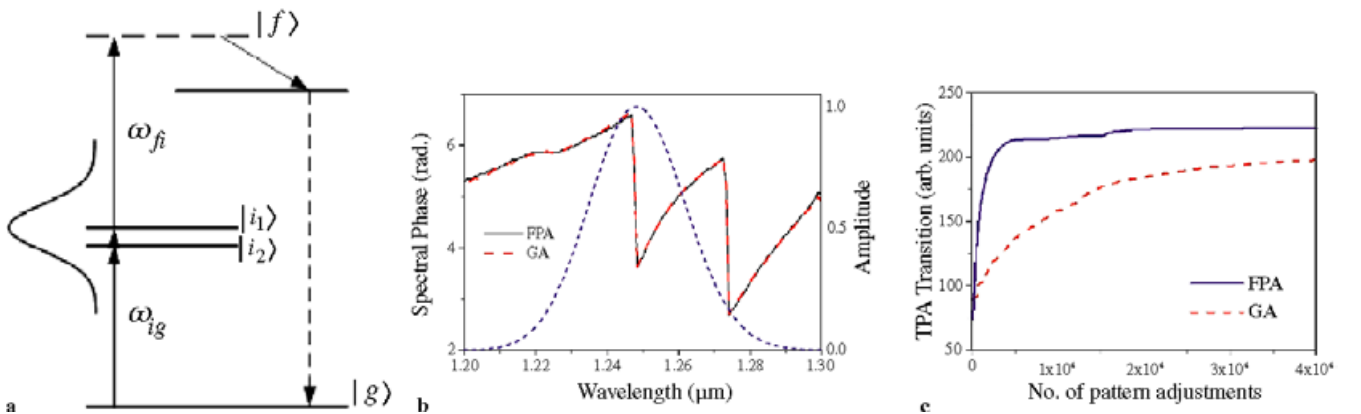
FIGURE 3 (**a**) Energy-level diagram of two-photon fluorescence (TPA) process. Two intermediate levels, $|i_1\rangle$ and $|i_2\rangle$, at 1247 nm and 1273 nm are assumed to lie within the spectral range of the input ultrashort pulse (see the dotted curve in Fig. 3b). (**b**) The phase profiles obtained with freezing phase algorithm (FPA: *solid line*) and genetic algorithm (GA: *dashed curve*) by maximizing the two-photon absorption probability. (**c**) Calculated TPA probability is plotted as a function of the number of spectral-phase profile adjustments with FPA (*solid curve*) and GA (*dash curve*)

The genetic algorithm is implemented with a population size of 200, which comprises of 90 fittest individuals from the previous generation, 10 randomly generated individuals, 60 from cross operation, and 40 from mutation of the 90 fittest parents. The simulated results are presented in Fig. 3b. The optimum spectral phase profiles deduced from GA and FPA are nearly identical. As shown in Fig. 3c our FPA scheme can yield the result with a faster speed. For practical applications, noise influences are also a crucial factor. In this regard, GA was found to be more sensitive to the fluctuation of laser power. This is because as the laser power decreases, GA tends to judge all individuals after this power reduction to be poorer than that of the previous generation. This erroneous judgment does not happen with the freezing phase algorithm.

The TPA amplitude without an intermediate resonant level can be expressed as

$$a_{\mathrm{f}}^{\mathrm{nr}} \approx -\frac{1}{i\hbar^2} \sum_n \left[\frac{\mu_{\mathrm{fn}}\mu_{\mathrm{ng}}}{\omega_{\mathrm{ng}} - \omega_{\mathrm{fg}}/2} \int_{-\infty}^{+\infty} E(\omega) E(\omega_{\mathrm{fg}} - \omega) d\omega \right]. \quad (7)$$

The optimal phase profiles obtained with GA and FPA were found to be a linear function of wavelength. As pointed out above, a linear spectral phase only results in a temporal shift of the entire pulse. Thus based on the time invariance principle, we can remove the linear phase term without losing any information about pulse characteristics. Therefore TPA without an intermediate resonant level can be maximized with a transform-limited pulse. Since all the spectral components of a TLP have the same phase, the TPA amplitude is contributed constructively from all pairs of spectral components with sum frequency being ω_{fg}.

3   Experimental section

3.1   *Phase retrieving from second-harmonic modulation pattern*

Figure 1 shows the schematic of an adaptive pulse shaping apparatus used in this study. The laser system is a Cr^{4+}: forsterite laser (from Avesta Project, Ltd.) pumped by a diode-pumped Yb: fiber laser (IPG Photonics, Ltd.). A typical output of the Cr^{4+}: forsterite laser was 280 mW of average power at a repetition rate of 76 MHz with a 7.5-W pump. The central wavelength is 1.252 μm and a typical full-width-at-half maximum (FWHM) bandwidth was approximately 42 nm, corresponding to 50-fs pulse duration.

The pulse is tailored by a pulse shaper consisting of a pair of gratings (600 g/mm), two concave reflectors with a focal length of $f = 10$ cm, and a liquid crystal SLM (Cambridge Research and Instrumentation Inc., Woburn, MA). The SLM consists of 128 97-μm-wide pixels, with a 3-μm gap between adjacent pixels. After reassembled by the output grating Gr2, the shaped pulse is focused onto a test sample. The phase distortion in the reflected pulse can be pre-compensated by the SLM. This leads to an optical pulse with constant phase before a 3-mm thick type-I β-Ba₂BO₄ (BBO) SHG crystal and generates a maximum SH signal. Here we effectively combine BBO SHG with a photodiode to offer a functionality of constant phase detection. The photodiode signal is sent to a computer to yield a phase compensating pattern with our freezing-phase algorithm.

To experimentally verify the function of FPA we first divide the SLM pixels into two groups: the first group, which involves three neighboring pixels, plays the role of phase modulation. The other group, which contains the remaining 125 pixels, is used as the reference. The phase of the modulation group is then varied from 0 to 2π for maximizing the SH intensity. The procedure is repeated by regrouping the SLM pixels until the phase retardations of all pixels are properly adjusted.

The experimentally measured SHG signal generated by an optical pulse reflected from a gold-coated mirror is shown in Fig. 4a. For reference, the spectrum of the mode-locked laser pulse is also plotted along the y-axis to mark the corresponding wavelengths of the SLM pixels. The SHG modulation patterns yield information about the phase distortion of the optical pulse. The experimental result reported here also confirms the prediction of Eq. (5) that the SHG modulation

a   **b**
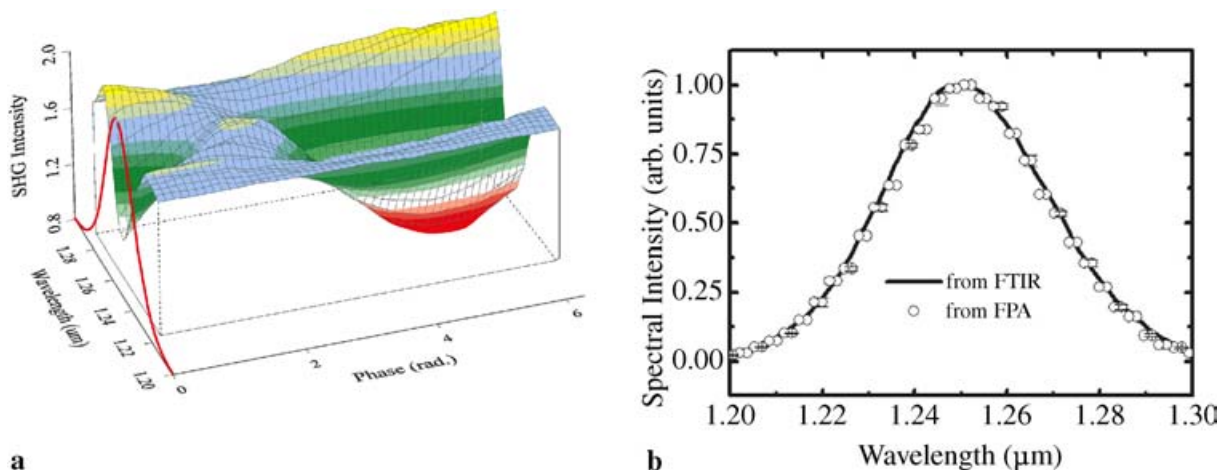
FIGURE 4   (**a**) Measured SHG signal with an optical pulse reflected from a gold-coated mirror is plotted as a function of the phase retardation of the phase modulation group of three consecutive pixels and their corresponding wavelength in a 4-f pulse shaper apparatus. (**b**) Spectral-phase sensitivity plot of SHG deduced from freezing-phase algorithm (FPA, *open circles*) and the optical pulse spectrum measured with Fourier-transformed infrared spectroscopy (FTIR, *solid line*)

sensitively depends on the amplitude of the spectral components chosen. Once the pixels lie outside the spectral range of the optical pulse, the SH intensity modulation is no longer observable.

We can define a spectral-phase sensitivity of SHG to be the difference between the maximum and minimum of the SH signal variation pattern (see Fig. 4a) when the phase retardation of the specific pixels is varied from 0 to 2π. Figure 4b presents a direct comparison of the deduced SHG spectral-phase sensitivity curve and that measured with Fourier-transformed infrared spectroscopy (FTIR). An excellent agreement was found, indicating that our adaptive phase compensation scheme can yield not only the spectral phase profile but also the spectral amplitude of a coherent optical pulse.

3.2   *Optical characteristics of the SBR device*

The SBR device used for this study comprises of self-assembled InAs quantum-dots embedded in a half-wave-thick (QD-$\lambda/2$) GaAs layer on a distributed Bragg reflector (DBR) stack. The device structure is depicted in Fig. 5a. The DBR of the device contains 21-periods stack with $\Lambda_1 = 97$ nm/$\Lambda_2 = 112$ nm GaAs/Al$_{0.92}$Ga$_{0.08}$As, which yields high reflection near $\lambda_B = 2(n_1\Lambda_1 + n_2\Lambda_2) \sim 1.3$ µm as shown in Fig. 3c.

The SBR exhibits two photoluminescent features with one centering at 867 nm (see Fig. 6a) and the other near 1250 nm (Fig. 6b) when the device is excited by a picosecond pulsed laser tunable from 450 nm to 1200 nm. The sharper profile at the long wavelength side of the 867-nm PL peak reflects the density of states near the conduction band edge and suggests the PL peak to be from GaAs of the DBR layers (i.e., the ω'-transition of Fig. 5b). The observed two PL peaks at 1235 nm and 1254 nm shall come from the self-assembled InAs QD layer (the Ω-transition of Fig. 5b). When the excitation wavelength is shorter than 1 µm, a broad background shows up in the long-wavelength PL, which can be ascribed to from recombination of photo-excited carriers in the quasi-2D InAs wetting layer [22].

Photo-luminescence excitation (PLE) can be modeled by means of 3-step processes: pulse excitation, intraband relaxation and recombination. If the intraband relaxation is much faster than radiative recombination rate, quasi-equilibrium distribution can be always achieved before radiative recombination. In this case, PLE is equivalent to single-photon absorption spectrum.

4   Results
4.1   *Coherent and incoherent multiphoton processes in SBR*

Equation (7) shows that the SHG field amplitude without an intermediate resonant level can be simplified to be

$$E_{\text{SHG}}(2\omega) \propto \int E(\Delta)E(2\omega - \Delta)d\Delta. \qquad (8)$$

In this case, SHG signal can be generated by all pairs of photons lying within the input field spectrum with a sum-frequency of 2ω. Similarly for third harmonic generation
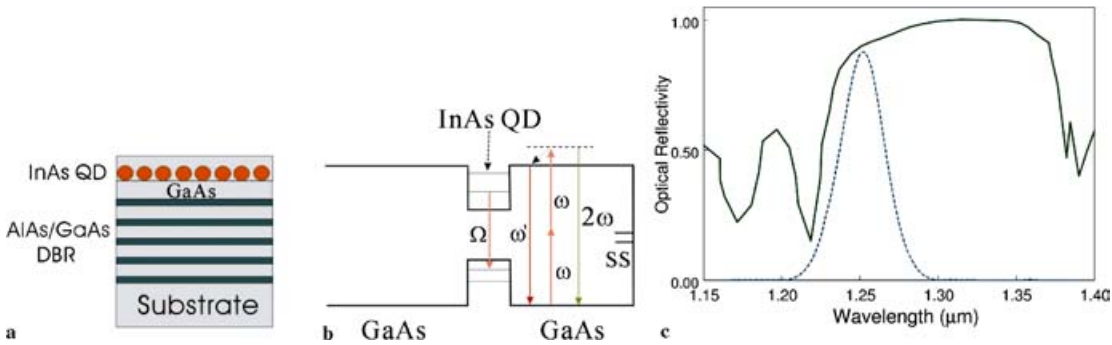

FIGURE 5 (**a**) Device structure of InAs quantum-dot SBR and (**b**) the corresponding diagram of electronic structure and optical transitions. (**c**) Measured optical reflectivity (*solid curve*) of the SBR and the spectral profile (*dashed line*) of an ultrashort laser used in this study
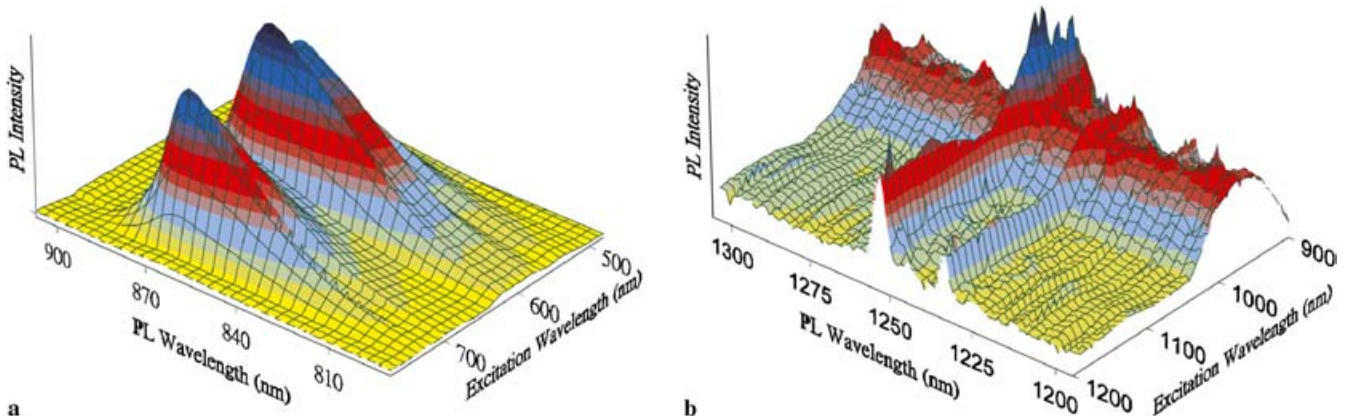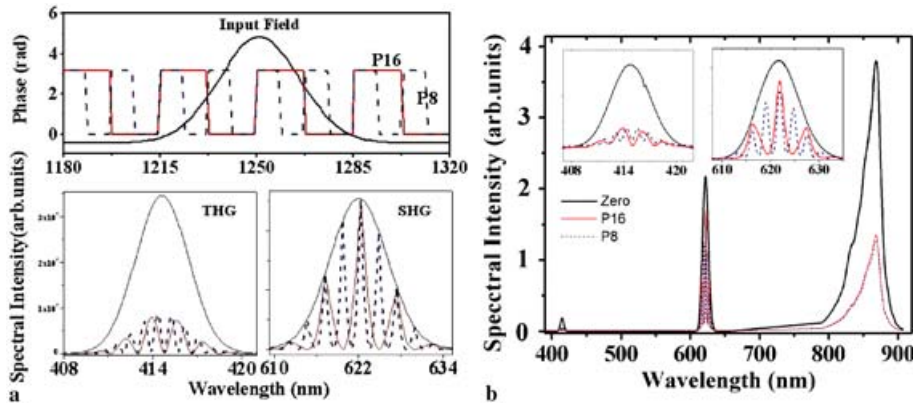

**FIGURE 6** Single-photon excited PL spectra of InAs quantum-dot SBR at a spectral range of (**a**) 800–900 nm, and (**b**) 1200–1300 nm

(THG), the THG amplitude can be expressed as

$$E_{THG}(3\omega) \propto \int E_{SHG}(2\omega - \Delta) E(\Delta) d\Delta. \tag{9}$$

Equations (8) and (9) can be used to calculate SHG and THG signals of a femtosecond input pulse at 1.25 μm. The input pulse is assumed to have a spectral profile shown in Fig. 7a. We modulate the input pulse with two periodic phase patterns P8 and P16. The calculated spectra of the SHG and THG signals from the phase modulated pulses are presented in Fig. 7a. The experimental results of the InAs-QD SBR excited by the same phase-modulated pulses are presented in Fig. 7b. The agreement is excellent, indicating that SHG ($\lambda \sim 628$ nm) and THG ($\lambda \sim 419$ nm) from the InAs-QD SBR shall not involve any intermediate resonant level. The two phase-modulated excitation pulses however do not produce distinctive difference in the peak near 868 nm. This suggests the peak to be originated from the two-photon fluorescence (TPF) of GaAs layers, where an energy relaxation process is involved to scramble the phase correlation of multiphoton nonlinear optical process before the output TPF photons at 868-nm are emitted.

4.2   *Spectral-Phase sensitivity plot of SHG signal*

The spectral-phase sensitivity plot of SHG and the optimum phase pattern to generate maximal SHG signal are presented in Fig. 8. A small dip at 1.253 μm in the spectral
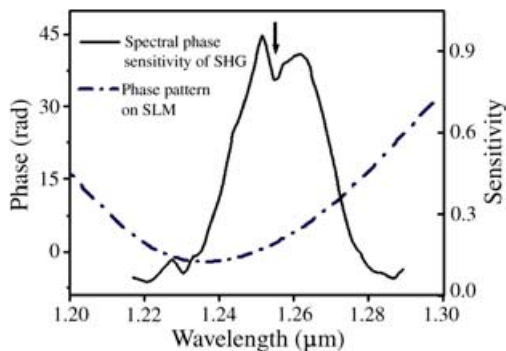
FIGURE 8   The optimum phase profile (*the dashed line*) of a femtosecond optical pulse which can yield maximum SHG signal. The spectral-phase sensitivity of SHG from the InAs QD SBR obtained with freezing phase scheme is presented as *solid curve*

phase sensitivity plot can be observed. The wavelength of the dip is equal to one of the PL peaks from InAs QDs shown in Fig. 4b. Note that under conditions of strong excitation, the absorption by InAs QDs is saturated because initial states of the transition are depleted while the final states are partially occupied. This shall lead to higher transmittance near 1.253 μm and therefore an increase instead of a dip in the spectral phase sensitivity curve. A plausible explanation for the dip is ultrafast resonant light scattering/emission by InAs QDs, which partially destroys the phase correlation but does not reduce the number of photons near 1.253 μm. As shown in Fig. 7, the SH signal generated from DBR stack is phase sensitive, therefore this partial phase de-correlation can decrease the SH signal.

### 4.3   *Coherent controlled multiphoton microscopy*

In Fig. 9 we present a comparison of TPF images of the InAs QD-λ/2 SBR. The first image was acquired over a 44 μm × 36 μm region with shaped pulses by resetting all SLM pixels to zero phase retardation (Fig. 9a). The image shown in Fig. 9b was taken over a slightly expanded region of 70 μm × 40 μm with femtosecond laser pulses shaped by the phase pattern that yields the maximal TPF signal. Three times increase in the image contrast can be achieved with coherent control.

Two sites in this scan region, which are labeled with P and S, are subjected to further study. The position P denotes a defect that yields higher TPF. We can use TPF signal from the P site or S site as the coherent control signal. The image shown in Fig. 9b is a two-dimensional distribution of TPF at 868 nm by using a phase profile (S′) to maximize the TPF signal from the S site, while the image shown in Fig. 9c is the same scan but using a phase pattern (P′) to maximize the P-site TPF signal.

Similar to the SHG study, we can also define the TPF spectral-phase sensitivity as the modulation depth of TPF signal when a spectral phase component of the excitation pulse is chosen to vary from 0 to 2π. The dotted and the dashed curves in Fig. 10a represent the spectral-phase sensitivity plot of TPF from the S and P sites, respectively. The spectral-phase sensitivity at the P site peaks at 1.25 μm, which is about 10 nm blue shift from that at the S-site. The corresponding TPF spectra are presented in Fig. 10b, where the P-site TPF spectrum was found to peak at 886 nm, while the S-site spectral peak
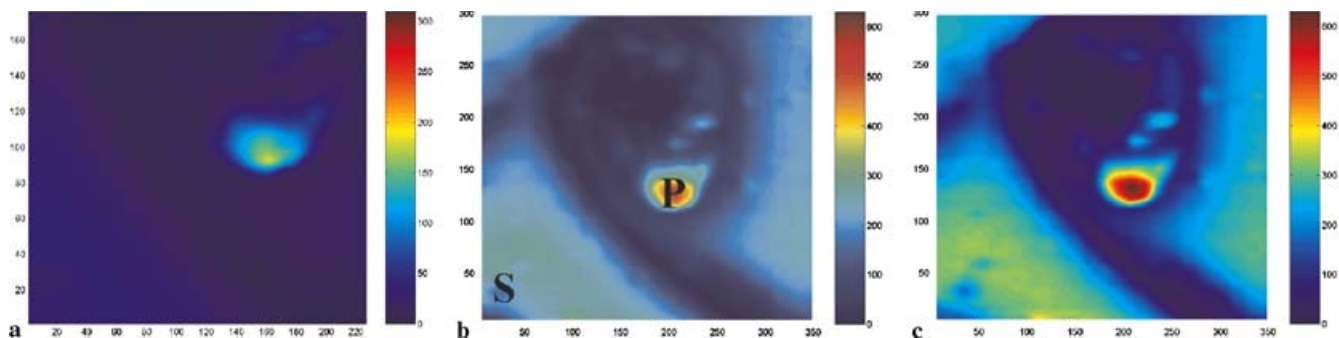
FIGURE 9 (**a**) TPF image on an area ($44\,\mu m \times 36\,\mu m$) of the InAs QD SBR. The sample is excited with femtosecond pulses by resetting all SLM pixels to zero phase retardation. (**b**) A TPF image ($70\,\mu m \times 60\,\mu m$) at 868 nm taken with the coherent control phase pattern S'. (**c**) TPF image was acquired with the coherent control phase pattern P'
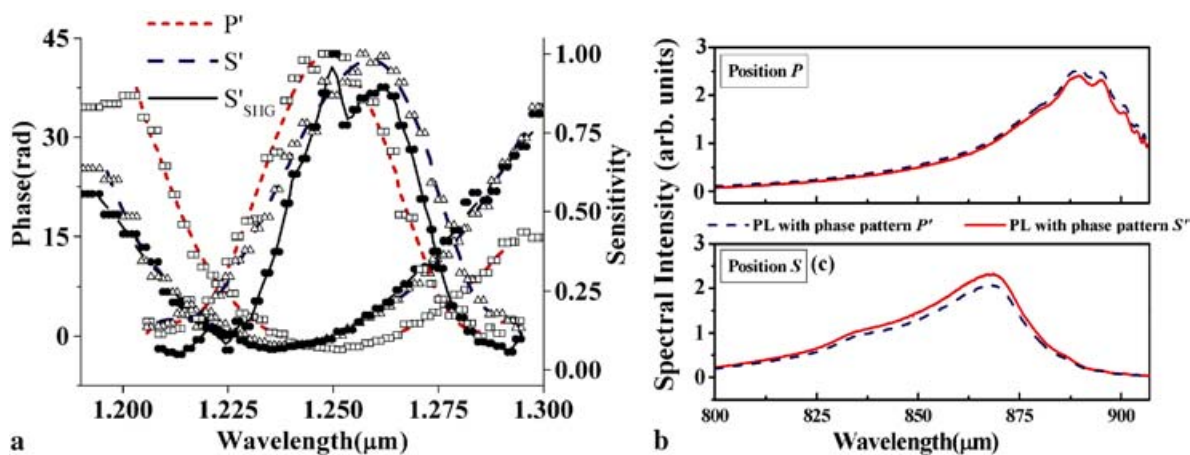
FIGURE 10 (**a**) Spectral-phase sensitivity curves of two-photon fluorescence (TPF) and the spectral-phase patterns used to yield maximum TPF signal from the position P (*short dashed*) and S (*dashed*). The same data shown in Fig. 8 for SHG (*solid curve*) are also included for comparison. TPF spectra from the position (**b**) P, and (**c**) S are presented. The spectra show that higher TPF signal can generate from position P and S with the phase patterns P' and S', respectively

locates at 868 nm. The 18-nm red-shift of the TPF spectrum at the P-site could originate from a localized strained GaAs structure with modified conduction band. The coherent control enhancement is verified by using the S'-phase profile, the 868-nm TPF signal is found to be higher than that used P'-phase profile. On contrast a higher 886-nm signal is obtained with the P' phase profile. No dip at $1.253\,\mu m$ was found in the TPF spectral-phase sensitivity curves, which supports that our interpretation of the origin of the dip in the SHG spectral-phase sensitivity curve.

The two phase patterns S' and S'_{SHG} that maximize TPF and SHG at the S-site are almost identical (see the dashed and the solid curves in Fig. 10a). The excited-state amplitude generated from two-photon excitation process serves as the common source of SHG and TPF. The two signals differ only on the emission process. SHG is a coherent process, while for TPF the emission is incoherent. The difference between SHG and TPF is very similar to the case of resonant Raman scattering and hot luminescence.

In summary, we have developed a freezing phase algorithm for adaptive coherent control with a femtosecond pulse shaper. Our theoretical study reveals that the freezing phase scheme can yield optimum spectral phase profile for second-harmonic generation (SHG), third-harmonic generation (THG), two-photon absorption (TPA) processes no matter an intermediate single-photon resonant level being in-

volved or not. In our study, the new scheme appears to be faster and has higher noise immunity than genetic algorithm. This freezing phase scheme had been employed for analyzing multiphoton processes in InAs quantum dot saturable Bragg reflector (SBR). Our results show that the function of InAs quantum dots can be revealed in the spectral-phase sensitivity plot of second harmonic signal. Coherent control contrast enhancement as large as a factor of three can be achieved at regions where the spectral peak wavelengths differ only 18 nm. Coherent control study offers an additional degree of freedom for distinguishing coherent and incoherent nonlinear optical processes. Our results suggest the new freezing phase scheme to be useful for various applications which require complete-field characterization and coherent control on one setup.

REFERENCES

1 R.S. Judson, H. Rabitz: Phys. Rev. Lett. **68**, 1500 (1992)
2 N. Dudovich, B. Orion, Y. Silberberg: Nature **418**, 512 (2002)
3 T. Brixner, N.H. Damrauer, P. Niklaus, G. Gerber: Nature **414**, 57 (2001)
4 I. Pastirk, J.M. Dela Cruz, K.A. Walowicz, V.V. Lozovoy, M. Dantus: Opt. Express **11**, 1695 (2003)

5 D. Yelin, D. Meshulach, Y. Silberberg: Opt. Lett. **22**, 1793 (1997)
6 D. Meshulach, D. Yelin, Y. Silberberg: J. Opt. Soc. Am. B **15**, 1615 (1998)
7 T. Baumert, T. Brixner, V. Seyfried, M. Strehle, G. Gerber: Appl. Phys. B **65**, 779 (1997)
8 E. Zeek, R. Bartels, M.M. Murnane, H.C. Kapteyn, S. Backus: Opt. Lett. **25**, 587 (2000)
9 A. Efimov, M.D. Moores, N.M. Beach, J.L. Krause, D.H. Reitze: Opt. Lett. **23**, 1915 (1998)
10 J. Kunde, B. Baumann, S. Arlt, F. Morier-Genoud, U. Siegner, U. Keller: Appl. Phys. Lett. **77**, 924 (2000)
11 C. Daniel, J. Full, L. Gonzalez, C. Lupulescu, J. Manz, A. Merli, S. Vajda, L. Woste: Science **299**, 536 (2003)
12 M.M. Wefers, K.A. Nelson: J. Opt. Soc. Am. B **12**, 1343 (1995)
13 A.M. Weiner: Rev. Sci. Instrum. **71**, 1929 (2000)
14 A. Assion, T. Baumert, M. Bergt, T. Brixner, B. Kiefer, V. Seyfried, M. Strehle, G. Gerber: Science **282**, 919 (1998)
15 W.S. Warren, H. Rabitz, M. Dahleh: Science **259**, 1581 (1993)
16 T.C. Weinacht, J.L. White, P.H. Bucksbaum: J. Phys. Chem. A **103**, 10 166 (1999)
17 R.J. Levis, G.M. Menkir, H. Rabitz: Science **292**, 709 (2001)
18 C.J. Bardeen, V.V. Yakovlev, K.R. Wilson, S.D. Carpenter, P.M. Weber, W.S. Warren: Chem. Phys. Lett. **280**, 151 (1997)
19 R. Mizoguchi, K. Onda, S.S. Kano, A. Wada: Rev. Sci. Instrum. **74**, 2670 (2003)
20 U. Keller: Nature **424**, 831 (2003)
21 D. Meshulach, Y. Silberberg: Phys. Rev. A **60**, 1287 (1999); N. Dudovich, Y. Silberberg: Phys. Rev. Let. **86**, 47 (2001)
22 C. Kammerer, G. Cassabois, C. Voisin, C. Delalande, P. Roussignol: Phys. Rev. Lett. **87**, 207 401 (2001)